Cellular interface morphologies in directional solidification. The one-sided model

Lyle H. Ungar and Robert A. Brown*
Department of Chemical Engineering and Materials Processing Center, Massachusetts Institute of Technology, Cambridge, Massachusetts 02139
(Received 19 August 1983)

Results of the shape and stability of finite-amplitude cellular interfaces arising in directional solidification are reported for a binary alloy described by a "one-sided" solidification model in which an imposed temperature gradient is unaffected by changes in interface shape. Asymptotic results valid for slightly deformed melt-solid interface shapes describe both smooth and sudden transitions to cellular interfaces in terms of supercritical and subcritical bifurcations with decreasing temperature gradient. Computer-implemented perturbation methods are combined with finite-element approximations of interface shape and concentration field to verify the asymptotic results for small-amplitude cells and extend the analysis to highly deformed interfaces. Numerical results predict that at large amplitudes, families of cellular interfaces which first evolved unstably toward increased temperature gradient reverse direction and regain stability. A discontinuous change in the stable interface morphology with an effective halving of its spatial wavelength is predicted to occur for highly deformed interfaces by secondary bifurcation between two neighboring shape familes and is related to the existence of second-order critical points for the onset of cellular forms.

I. INTRODUCTION

Morphological stability theory describes the tendency of a microscopically planar solidification front separating a binary melt from its solid to develop undulations that eventually lead to cellular and dendritic crystal growth. The physics describing the onset of these undulations, known as constitutional supercooling, was first laid out by Rutter and Chalmers[1] in terms of the quasistatic interface. As a binary crystal freezes from an otherwise quiescent melt, solute is rejected at the interface (corresponding to an equilibrium segregation coefficient k less than unity) and diffuses into the bulk melt at concentration $\tilde{c}_\infty$. The increase in concentration decreases the freezing point of melt adjacent to the interface, and, depending on the temperature gradient there, may lead to the spatially irregular freezing of melt ahead of the initially planar front.

Mullins and Sekerka[2,3] used linear theory to analyze the stability of a flat melt-solid interface with respect to small shape disturbances and obtained the exact relationship between the critical temperature gradient $\tilde{G}$ at the onset of the instability, the spatial wavelength $\tilde{\lambda}$ of the disturbance, and other thermophysical parameters. For temperature gradients less than a minimum value $\tilde{G}$ ($\equiv \tilde{G}_c$), disturbances with a continuous range of wavelengths $\tilde{\lambda}_1(\tilde{G}) < \tilde{\lambda} < \tilde{\lambda}_2(\tilde{G})$ were found to be unstable, with only perturbations having the limiting values of $\tilde{\lambda}$ being neutrally stable. At $\tilde{G} = \tilde{G}_c$, a single disturbance is neutrally stable and planar interfaces grown in any gradient above this value are stable to small-amplitude fluctuations.

Since this pioneering work, linear stability analysis has been applied to planar interfaces solidifying under a myriad of conditions (see the review by Delves[4]), but only a few studies[5-7] have addressed the question of the morphology of the interface beyond the point of incipient instability of the planar shape. The intricate patterns seen during cellular and dendritic solidification point to the rich mathematical structure that must be described by models of the solidification of a constitutionally unstable binary alloy. In this and two related papers, we present asymptotic and computer-aided analysis of the shape and stability of cellular interfaces for a model solidification system in the hope of elucidating some of this structure.

We study a binary crystal solidifying into a static melt in which the thermal properties of both phases are constant with temperature and identical, and where the latent heat of solidification is negligible. These assumptions lead to the "one-sided" model for solidification employed by others;[8,9] here the temperature field is described solely by its gradient near the interface and is independent of growth rate and morphology. Since the temperature field is decoupled from the free-boundary problem that governs interface shape, the complexity of both asymptotic and numerical analysis is greatly reduced. Moreover, the one-sided model is appropriate for qualitatively describing many metallic and semiconductor systems at slow growth rates; it is described in Sec. II.

Our analyses follow the approach of bifurcation theory and trace families of interface morphologies in terms of parameters such as the applied temperature gradient and the crystal growth rate. The asymptotic analysis is founded on expansion of the interface shape in terms of its deviation from planarity and so is limited to forms that differ only mildly from the flat configuration. The numerical analysis combines a newly developed finite-element method for solution of free-boundary problems[10] with computer-implemented perturbation techniques for tracking families of steadily growing interface shapes,[11,12] and for determining their stability.[13] These techniques are described fully elsewhere and the application to the one-sided solidification model is only sketched in Sec. IV.

The earliest treatment of the nonlinear evolution of con-

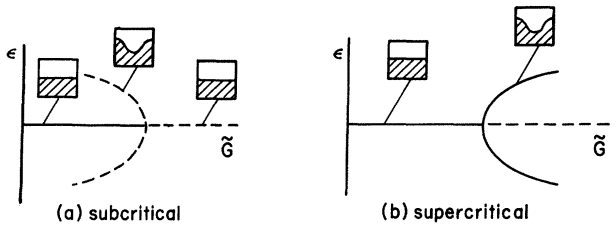

FIG. 1. Characterization of weakly nonlinear cellular melt-solid interfaces as either (a) subcritical or (b) supercritical bifurcation in terms of $\tilde{G}$ from the planar shape.

stitutionally unstable solidification interfaces was the asymptotic analysis of Wollkind and Segel.[5] These authors used an expansion correct to second order in the amplitude of the deformed interface to examine the shape and stability of the weakly nonlinear cellular morphologies for a model binary alloy without heat generation at the melt-solid interface. Two types of interface behavior were discovered, depending on the value of the growth rate and other thermophysical parameters. For low growth rates cellular interfaces existed only for values of the temperature gradient $\tilde{G}$ greater than $\tilde{G}_c$ and were unstable to small-amplitude perturbations. At high growth rates the deformed interfaces evolved toward lower values of $\tilde{G}$ and were stable. These two cases are classified in Fig. 1 as sub- and supercritical bifurcations from the family of planar shapes with ϵ representing a measure of the amplitude of the deformed interface; $\epsilon=0$ corresponds to the planar shape. When the cellular forms bifurcated toward higher values of $\tilde{G}$ (the subcritical case) the analysis in Ref. 5 yielded no prediction for the shape and spatial frequency of steady-state interface shapes that may exist for temperature gradients less than the value of neutral stability.

Langer[7] analyzed the cellular interface shapes predicted for a symmetric model of solidification where the diffusivity of solute is equal in both melt and solid. His work gives some indication of the fate of cellular interfaces that evolve subcritically in $\tilde{G}$ initially. By continuing an asymptotic analysis to cubic interactions in the amplitude, Langer traced similar shape families to the point where they eventually reversed direction toward lower values of $\tilde{G}$ and regained stability. The results presented in Sec. V show the same behavior for the one-sided solidification model.

Langer's analysis also predicted other interesting features of the cellular families. The amplitude of interfaces with set wavelength passed through a maximum and then decreased with decreasing $\tilde{G}$ until a new minimum value of the temperature gradient was reached where the family ended discontinuously. We show in Sec. V that both phenomena are predicted by the one-sided model, and that the ending of the interface family described by Langer marked, in our representation, the connection between two families of interfaces with wavelengths $\tilde{\lambda}$ and $\tilde{\lambda}/2$, respectively. As shown below, this connectivity gives a qualitative description for the change in frequency of cellular interfaces with decreasing temperature gradient as a secondary bifurcation point between two families of

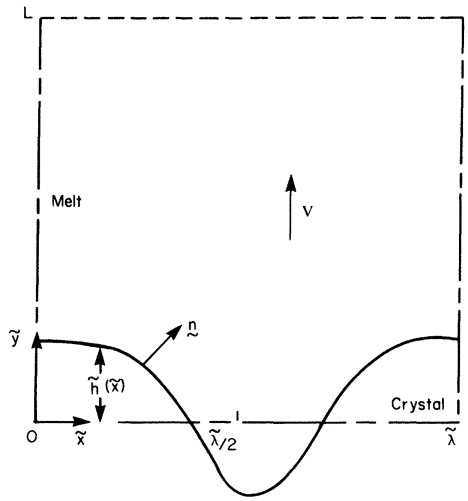

FIG. 2. Schematic of melt-solid interface in a unidirectional solidification system. Wavelength of the cells is denoted as $\tilde{\lambda}$.

interface shapes and links the existence of second-order bifurcation points at particular values of $\tilde{G}$ and wavelength. The connection between multiple bifurcation at a second-order critical point and secondary bifurcation between neighboring families is well known in reaction-diffusion[14] and hydrodynamic[15,16] problems.

II. ONE-SIDED SOLIDIFICATION MODEL AND LINEAR STABILITY ANALYSIS

We view unidirectional solidification of a binary melt from a reference frame attached to a planar melt-solid interface moving at the constant velocity V. The shape of the interface and the field quantities, e.g., temperature and composition, in melt and solid, are described in the Cartesian-coordinate system shown in Fig. 2. The melt-solid interface is located at $y=h(\tilde{x},\tilde{t})$ and the vector field $\vec{n}$ everywhere normal to this interface is

$$\vec{n}=\frac{\vec{e}_y-\vec{e}_x\tilde{h}_{\tilde{x}}}{(1+\tilde{h}_{\tilde{x}}^2)^{1/2}}\ , \tag{2.1}$$

where $\tilde{h}_{\tilde{x}}\equiv\partial\tilde{h}/\partial\tilde{x}$ and $\vec{e}_x,\vec{e}_y$ are unit vectors.

Unidirectional solidification takes place when the temperature gradient far from the interface is parallel with the growth direction and is constant with distance from the solidification front. In this case, the temperature field near the interface is determined entirely by temperature gradients in the melt and solid. In a typical melt and crystal of metal or semiconductor, heat transfers mainly by conduction and is much more rapid than solute transfer. Then, if the thermal conductivities of melt and crystal are similar and the latent heat released upon solidification is small, the imposed temperature gradient will be constant through both melt and crystal and will not be altered by changes in the shape of the melt-solid interface. We refer to this solidification melt as one sided[8,9] in the sense that the shape of the melt-solid interface is set solely by the deformation of the solute composition field in the

melt and its interaction with the imposed temperature field

$$T(\tilde{y})=T_m^0+\tilde{y}\tilde{G}\ , \tag{2.2}$$

where T_m^0 is the melting temperature of the planar interface located at $\tilde{y}=\tilde{h}(\tilde{x})=0$. The one-sided model is a special case of the more general formulation considered by Wollkind and Segal.

When bulk convection is absent the distribution of solute in the melt $\tilde{c}(\tilde{x},\tilde{y},\tilde{t})$ is governed by the conservation equation

$$\frac{\partial\tilde{c}}{\partial\tilde{t}}=\mathscr{D}\nabla^2\tilde{c}+V\frac{\partial\tilde{c}}{\partial\tilde{y}}\ , \tag{2.3}$$

where $\mathscr{D}$ is the diffusion coefficient and

$$\nabla^2(\tilde{c})\equiv\frac{\partial^2\tilde{c}}{\partial\tilde{x}^2}+\frac{\partial^2\tilde{c}}{\partial\tilde{y}^2}$$

is the Laplacian operator. The solute balance equation (2.3) is solved inside a slice of melt $(0\le\tilde{x}\le\tilde{\lambda},\tilde{h}\le\tilde{y}\le\infty)$ along the boundaries of which

$$\frac{(V+\partial\tilde{h}/\partial\tilde{t})\tilde{c}(k-1)}{(1+\tilde{h}_{\tilde{x}}^2)^{1/2}}=\mathscr{D}\,\vec{n}\cdot\nabla\tilde{c},\quad \tilde{y}=\tilde{h}(\tilde{x},\tilde{t}),\quad 0\le\tilde{x}\le\tilde{\lambda} \tag{2.4}$$

where k is the equilibrium (subscript eq) partition coefficient for solute between melt and crystal at the interface, i.e., the composition of the crystal is

$$\tilde{c}_{s,\mathrm{eq}}(\tilde{x},\tilde{t})=\tilde{c}\,(\tilde{x},\tilde{h}(\tilde{x},\tilde{t}),t)k\ .$$

Along the sides of the slice and far away from it, the concentration field obeys

$$\tilde{c}(\tilde{x},\tilde{y},\tilde{t})=\tilde{c}_\infty,\quad \tilde{y}\to\infty,\quad 0\le\tilde{x}\le\tilde{\lambda} \tag{2.5}$$

$$\frac{\partial\tilde{c}}{\partial\tilde{x}}=0,\quad \tilde{x}=0,\tilde{\lambda},\quad \tilde{h}(\tilde{x},\tilde{t})\le\tilde{y}<\infty \tag{2.6}$$

where $\tilde{c}_\infty$ is the bulk composition of the melt.

The temperature at the solidification front is described by combining the idealized phase diagram with the Gibbs-Thomson[17] condition to yield

$$T_I(\tilde{x},\tilde{t})\equiv T(\tilde{x},\tilde{h}(\tilde{x},\tilde{t}),\tilde{t})=T_m^0+\tilde{m}\tilde{c}+T_m^0\tilde{\Gamma}(\mathscr{H})\ ,$$
$$\tilde{y}=\tilde{h}(\tilde{x},t),\quad 0\le\tilde{x}\le\tilde{\lambda} \tag{2.7}$$

in which $\tilde{m}$ is the slope of the solidus curve, $\tilde{\Gamma}$ is the surface free energy, $\tilde{T}_m$ is the melting temperature of the pure material at a planar melt-solid interface, and

$$2\mathscr{H}\equiv\frac{d^2\tilde{h}/d\tilde{x}^2}{[1+(d\tilde{h}/d\tilde{x})^2]^{3/2}}$$

is twice the mean curvature of the interface. Because the temperature field is not disturbed by interface deformation, Eq. (2.7) sets its location by

$$T_I=T_m^0+\tilde{G}h(\tilde{x},\tilde{t}),\quad 0\le\tilde{x}\le\tilde{\lambda}\ . \tag{2.8}$$

Equations (2.2)–(2.8) describe a mathematically nonlinear free- (steady-state) or moving- (time-dependent)

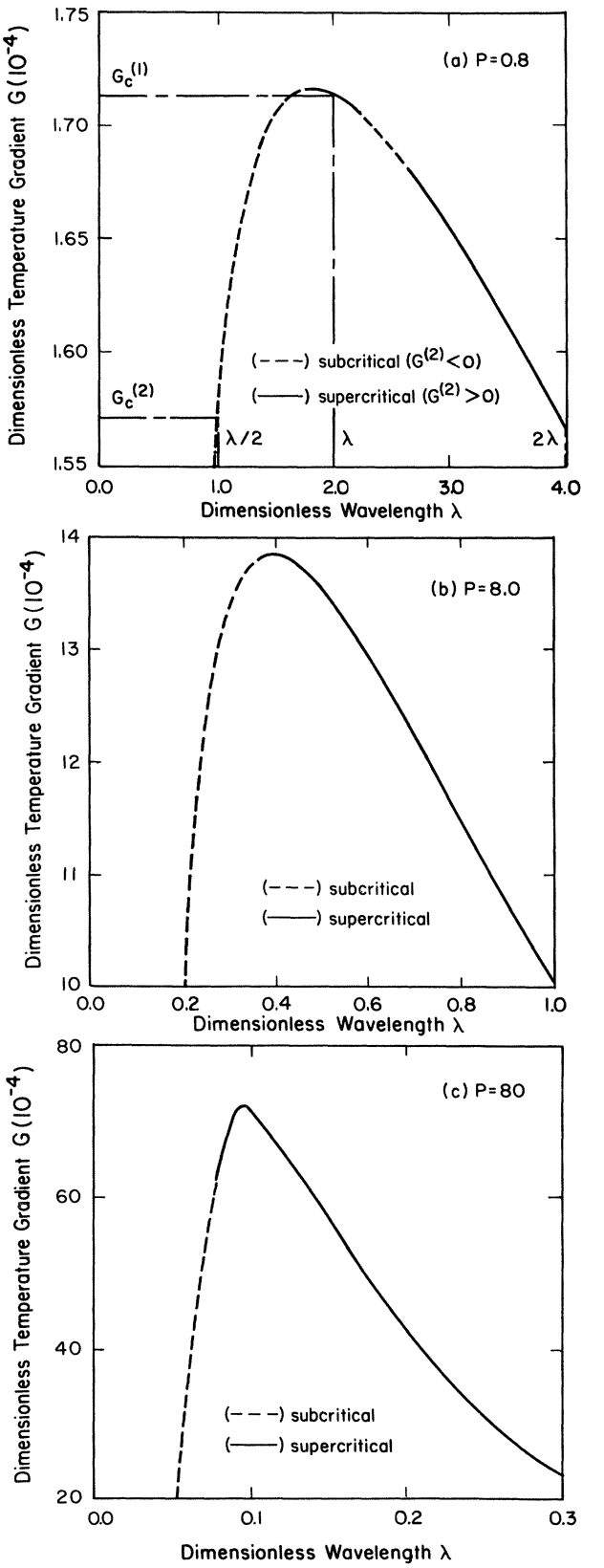

FIG. 3. Critical values of temperature gradient $G_c^{(1)}$ predicted as a function of wavelength for the Pb-Sb system. The sign of the coefficient $G^{(2)}$ is denoted by a solid or dashed curve. Curves are shown for Peclet numbers of (a) 0.8, (b) 8.0, and (c) 80.

boundary problem for the concentration field and interface shape. This problem has multiple steady-state solutions. The family with planar interfaces is the most easily obtained,

$$\tilde{h}_0(\tilde{x})=0\ , \tag{2.9a}$$

$$\tilde{c}_0(\tilde{y})=(c_\infty/k)\{1+(k-1)[1-\exp(-V\tilde{y}/\mathscr{D})]\}\ . \tag{2.9b}$$

We have followed the approach of Mullins and Sekerka,[2,3] and detect the bifurcation of cellular melt-solid interfaces from the planar form by examining the stability of the solutions (2.9) to small-amplitude disturbances of interface shape of the form $h(\tilde{x},\tilde{t})=\hat{h}(t)\cos\tilde{\omega}\tilde{x}$, where $\tilde{\omega}$ is its spatial wave number. Standard procedures for linear stability analysis yield a dispersion relation for the neutral stability of the disturbance with frequency ω satisfying the equation

$$T_m^0\tilde{\Gamma}\tilde{\omega}^2+\tilde{G}=\frac{\tilde{m}\tilde{c}_\infty(k-1)V(\tilde{\omega}^*-\tilde{V}/\mathscr{D})}{\mathscr{D}k[\tilde{\omega}^*+(k-1)\tilde{V}/\mathscr{D}]} \tag{2.10}$$

with

$$\tilde{\omega}^*\equiv(V/2\mathscr{D})+[(V/2\mathscr{D})^2+\tilde{\omega}^2]^{1/2}\ .$$

Result (2.10) is a special case of the dispersion equation in Ref. 2. Typical stability curves of temperature gradient versus wavelength are plotted on Fig. 3 in a dimensionless form defined in the next section. In a real solidification system, all frequencies are equally probable and stability of the planar front is first lost at the largest value of $\tilde{G}$, for fixed growth rate, at which the interface is unstable to at least one disturbance. This extremum is found from Eq. (2.10), which yields an implicit relationship for the spatial wave number $\tilde{\omega}_c$ for loss of stability as

$$(k-1)\tilde{V}c_\infty\tilde{m}/\tilde{\Gamma}\mathscr{D}(T_m^0)^2=[\tilde{\omega}_c^*+(k-1)\tilde{V}/\mathscr{D}]^2(2\tilde{\omega}_c^*-\tilde{V}/\mathscr{D})\ . \tag{2.11}$$

The critical value of the temperature gradient $\tilde{G}\equiv\tilde{G}_c$ is computed by substituting $\tilde{\omega}^*\equiv\tilde{\omega}_c^*$ into Eq. (2.10). We show in the remainder of this paper that a family of two-dimensional cellular interfaces evolves from the planar forms at this value of $\tilde{G}$, and we trace these shapes to large values of interface deformation.

III. WEAKLY NONLINEAR ANALYSIS

The steadily growing cellular interfaces which evolve from the neutrally stable value of the temperature gradient are computed by asymptotic methods presented in this section and by a finite-element analysis outlined in Sec. IV. These calculations are carried out for interface morphologies with discrete wavelengths $\tilde{\lambda}$. We concentrate on wavelengths near $\tilde{\lambda}=\tilde{\lambda}_c\equiv2\pi/\tilde{\omega}_c$, the value at which stability of the planar shape is first lost. Setting the wavelength of the interface is an idealization which disrupts the continuous spectrum for critical values of temperature gradient into discrete points $\{\tilde{G}_c^{(i)}\}$, each corresponding to disturbances with spatial wave numbers that are integer multiples of $\tilde{\omega}_c$. These discrete values are depicted on Fig. 3(a) in terms of the wavelength $\lambda\equiv\tilde{\lambda}/\lambda^*$ of the cellular forms.

The asymptotic analyses are carried out on a modified equation set formed from Eqs. (2.2)–(2.7) by subtracting out the concentration field (2.9) resulting from a planar interface and introducing dimensionless variables with length, temperature, and concentration scaled with λ^*, T_m^0, and $\tilde{c}_\infty$, respectively. These equations are in the melt $[0\le x\le\lambda,\ h(x)\le y<\infty]$

$$\nabla^2c+P\frac{\partial c}{\partial y}=\frac{\partial c}{\partial t}\ , \tag{3.1a}$$

at the melt-solid interface $[y=h(x),\ 0\le x\le\lambda]$,

$$Gh-m\frac{k-1}{k}[1-\exp(-Ph)]-mc-\Gamma\frac{\partial^2h}{\partial x^2}\left[1+\left[\frac{\partial h}{\partial x}\right]^2\right]^{-3/2}=0\ , \tag{3.1b}$$

$$\frac{\partial c}{\partial y}-\frac{\partial h}{\partial x}\frac{\partial c}{\partial x}-(k-1)P[c+1-\exp(-Ph)]=\frac{\partial h}{\partial t}\left[c+\frac{1}{k}+\frac{k-1}{k}[1-\exp(-Ph)]\right](k-1)\ , \tag{3.1c}$$

and along the other boundaries of the melt,

$$c(x,\infty)=0\ , \tag{3.1d}$$

$$\frac{\partial c}{\partial x}=\frac{\partial h}{\partial x}=0,\quad x=0,\lambda\ . \tag{3.1e}$$

In Eqs. (3.1), $P\equiv V\lambda^*/\mathscr{D}$ is the dimensionless growth rate or Peclet number, $\Gamma\equiv\tilde{\Gamma}/\lambda^*$ is the capillary constant, $G\equiv\tilde{G}\lambda^*/T_m^0$ is the dimensionless temperature gradient, and $m=\tilde{m}\tilde{c}_\infty/T_m^0$ is the slope of the phase diagram. The boundary conditions (3.1e) force the interface shape to have wavelength λ.

The cellular interfaces are calculated by standard techniques for analyzing bifurcations.[18] The interface shape, concentration field, and temperature gradient are expanded in an amplitude parameter ϵ which measures the difference between the planar and cellular forms. We follow the approach of domain perturbations[19] and account for the dependence of the concentration field $c(x,y)$ on the shape of the interface by introducing the change of coordinates $\eta\equiv y-h(x)$. The expansions are written as

$$\begin{bmatrix}c(x,y;\epsilon)\\h(x;\epsilon)\\G(\epsilon)\end{bmatrix}=\sum_{n=0}^{\infty}\frac{\epsilon^n}{n!}\begin{bmatrix}c^{[n]}(x,\eta)\\h^{(n)}(x)\\G^{(n)}\end{bmatrix}\ , \tag{3.2}$$

where

$$c^{[k]}(x,\eta)\equiv\frac{d^kc(x,\eta;0)}{d\epsilon^k}\ ,\qquad h^{(k)}(x)\equiv\frac{d^kh(x;0)}{d\epsilon^k},\quad G^{(k)}\equiv\frac{d^kG(0)}{d\epsilon^k}\ . \tag{3.3}$$

The planar interface is recovered as the trivial zeroth-order solution of the equation set, i.e., $c^{[0]}=0$, $h^{[0]}=0$

with $G^{(0)}$ unspecified. Each term in the expansion for the concentration $c^{[k]}(x,\eta)$ is expressed using the chain rule for differentiation as a sum of a contribution on the rectangular domain ($0\le x\le\lambda$, $0\le\eta<\infty$) and of terms that account for the deformation of the interface at each order of ϵ. The first four relationships are written as follows:

$$c^{[0]}(x,\eta)\equiv c^{(0)}(x,\eta)=0\ , \tag{3.4a}$$

$$\begin{aligned} c^{[1]}(x,\eta)&\equiv\frac{\partial c}{\partial\epsilon}(x,\eta;0)+h^{(1)}(x)\frac{\partial c}{\partial\eta}(x,\eta;0)\\ &\equiv c^{(1)}(x,\eta)+h^{(1)}(x)\frac{\partial c^{(0)}}{\partial\eta}=c^{(1)}(x,\eta)\ , \end{aligned} \tag{3.4b}$$

$$\begin{aligned} c^{[2]}(x,\eta)&\equiv c^{(2)}(x,\eta)+2h^{(2)}(x)\frac{\partial c^{(0)}}{\partial\eta}\\ &\quad+h^{(1)2}\frac{\partial^2 c^{(0)}}{\partial\eta^2}+2h^{(1)}(x)\frac{\partial c^{(1)}}{\partial\eta}\\ &=c^{(2)}(x,\eta)+2h^{(1)}\frac{\partial c^{(1)}}{\partial\eta}\ , \end{aligned} \tag{3.4c}$$

$$\begin{aligned} c^{[3]}(x,\eta)&=c^{(3)}(x,\eta)\\ &\quad+3\left[h^{(1)}\frac{\partial c^{(2)}}{\partial\eta}+h^{(2)}\frac{\partial c^{(1)}}{\partial\eta}+h^{(1)2}\frac{\partial^2 c^{(1)}}{\partial\eta^2}\right], \end{aligned} \tag{3.4d}$$

where

$$c^{(k)}(x,\eta)\equiv\frac{\partial c^k}{\partial\epsilon^k}$$

and is defined on the rectangular domain.

Substituting the expansions (3.4) into the governing equations (3.1) yields a sequence of linear problems for the set $(c^{(k)},h^{(k)},G^{(k-1)})$ formed by collecting terms of kth order in ϵ. The nonlinearities in the original equations and the couplings between the expansion coefficients both result entirely from the two boundary conditions (3.1b) and (3.1c). We focus on these two conditions by defining a linear operator for the interface shape and concentration $(h(x),c(x,0))$ as

$$\mathscr{L}\underline{u}_n\equiv\begin{bmatrix} G-\Gamma\dfrac{\partial^2}{\partial x^2}-\dfrac{m(k-1)P}{k} & -m\\ -(k-1)P^2 & \dfrac{\partial}{\partial y}-(k-1)P \end{bmatrix}\begin{bmatrix} h^{(n)}\\ c^{(n)}\end{bmatrix}=\underline{\rho}_n\ , \tag{3.5}$$

where $\underline{\rho}_n$ is a vector calculated at each order from the nonhomogeneous terms in Eqs. (3.1a) and (3.1b). The first three vectors $(\underline{\rho}_1,\underline{\rho}_2,\underline{\rho}_3)$ are needed for our analysis,

$$\underline{\rho}_1=\underline{0}\ , \tag{3.6a}$$

$$\underline{\rho}_2=-\begin{bmatrix} m(k-1)P^2h^{(1)2}/k-2h^{(1)}G^{(1)}-2mh^{(1)}c_\eta^{(1)}\\ -2h_x^{(1)}c_x^{(1)}+(k-1)P^3h^{(1)2}+2h^{(1)}c_{\eta\eta}^{(1)}-2(k-1)Ph^{(1)}c_\eta^{(1)}\end{bmatrix}, \tag{3.6b}$$

$$\underline{\rho}_3=-\begin{bmatrix} m(k-1)P^2(3h^{(1)}h^{(2)}-Ph^{(1)3})/k+9\Gamma h_{xx}^{(1)}h_x^{(1)2}+3G^{(1)}h^{(2)}\\ \quad+3G^{(2)}h^{(1)}-3m(h^{(1)}c_\eta^{(2)}+h^{(1)2}c_{\eta\eta}^{(1)}+h^{(2)}c_\eta^{(1)})\\ 3(-h_x^{(1)}c_x^{(2)}-h_x^{(2)}c_x^{(1)}+h^{(1)}c_{\eta\eta}^{(2)}+h^{(1)2}c_{\eta\eta\eta}^{(1)}+h^{(2)}c_{\eta\eta}^{(1)})\\ \quad-6h_x^{(1)}(h_x^{(1)}c_\eta^{(1)}+h_x^{(1)}c_{\eta x}^{(1)})+(k-1)(3h^{(1)}h^{(2)}-Ph^{(1)3})P^3\\ \quad-3(k-1)P(h^{(1)}c_\eta^{(2)}+h^{(1)2}c_{\eta\eta}^{(1)}+h^{(2)}c_\eta^{(1)})\end{bmatrix}, \tag{3.6c}$$

where subscripts denote partial differentiation. Equations (3.5) and (3.6) are solved with the field equation (3.1a) and boundary conditions (3.1d) and (3.1e) expanded to the appropriate order of ϵ.

The homogeneous equation set at first order in ϵ forms an eigenvalue problem for determining the critical values $\{G_0^{(n)}\}=\{G_c^{(n)}\}$ for bifurcation from the planar state. In dimensionless form, these eigenvalues and their corresponding eigenvectors are

$$G_0^{(n)}\equiv G_c^{(n)}=\frac{m(k-1)P(\omega_n-P)}{k(\omega_n+(k-1)P)}-\Gamma\omega_n^2\ , \tag{3.7}$$

$$\underline{u}_1^{(n)}\equiv\begin{bmatrix} h^{(1)}(x)\\ c^{(1)}(x,0)\end{bmatrix}=k_n\begin{bmatrix}1\\ \hat{C}_n\end{bmatrix}\cos(\omega_n x)\ , \tag{3.8}$$

where $\omega_n=2n\pi/\lambda$ is the wave number,

$$\hat{C}_n\equiv[(G_0^{(n)}+\omega_n^2\Gamma)k-(k-1)Pm]/mk\ ,$$

and k_n is a scalar amplitude which is set to 1.

The amplitude ϵ is defined as the deviation of the cellular interfaces from a plane as

$$\epsilon\equiv\langle\underline{u}(x;\epsilon),\underline{\Phi}_n^*(x)\rangle\ , \tag{3.9}$$

where $\langle\ ,\ \rangle$ denotes the surface inner product

$$\langle \underline{u}_1, \underline{u}_2 \rangle \equiv \frac{1}{\lambda}\int_0^{\lambda}(c_1c_2+h_1h_2)dx\ , \tag{3.10}$$

and $\underline{\Phi}^*$ is the eigenvector for the problem adjoint to (3.5) in the inner product (3.10). The adjoint problem is formulated by standard methods and is available in Ref. 20. The appropriate adjoint eigenvector for the eigenvalue $G_0^{(n)}$ is

$$\underline{\Phi}_n^* \equiv k_n^* \begin{bmatrix} 1 \\ \hat{C}_n^* \end{bmatrix} \cos(\omega_n x)\ , \tag{3.11}$$

with $C_n^* = -m/[\omega_n^* + (k-1)P]$ and k_n^* as a scalar amplitude. Applying the amplitude definition to $O(\epsilon)$ gives the standard biorthoganization of the eigenvectors as

$$\langle \underline{u}_1^{(n)}, \underline{\phi}_n^* \rangle = 1\ , \tag{3.12}$$

which determines the constants k_n^*.

Because the operator (3.5) is singular at critical values $\{G_0^{(n)}\}$, the nonhomogeneous problems which result at second and higher orders in ϵ are only solvable when the vectors $\{\underline{\rho}_n\}$ satisfy the orthogonality conditions

$$\langle \underline{\rho}_n, \underline{\phi}_m^* \rangle = 0\ , \tag{3.13}$$

where n is the order of the problem and m is the eigenpair on which the expansion is based. These conditions along with the amplitude definition, differential equations, and boundary conditions complete the set for calculating $h^{(n)}(x)$, $c^{(n)}(x,0)$, and $G^{(n-1)}$ for $n \geq 2$.

Solution of the order ϵ^2 problem gives the slopes of the bifurcating families and corrections to the interface shape and concentration field,

$$G_1^{(n)} = 0, \quad n = 1,2,\ldots \tag{3.14a}$$

$$\underline{u}_2^{(n)} = \begin{bmatrix} h^{(2)}(x) \\ c^{(2)}(x,0) \end{bmatrix} = \begin{bmatrix} H_{20} \\ C_{20} \end{bmatrix} + \begin{bmatrix} H_{22} \\ C_{22} \end{bmatrix} \cos(2\omega_n x)\ , \tag{3.14b}$$

where the coefficients H_{20}, H_{22}, C_{20}, and C_{22} are listed in the Appendix. Equation (3.14a) implies that each family of cellular forms branches vertically from the planar shapes. The direction of each family $\{G_2^{(n)}\}$ was determined after a long but straightforward calculation of the solvability condition at $O(\epsilon^3)$ to be

$$G_2^{(n)} = -\frac{1}{8kP^3}\{3k\omega_n^4\Gamma - 2\hat{C}_n\hat{C}_n^*\omega_n^2\omega_n^* + mP^2[k\hat{C}_n + (k-1)P]\}$$

$$+\frac{C_{20}}{2k^2}(m+k^2P\hat{C}_n)+\frac{C_{22}}{4k^2P}[m\omega_{2n}^*+k\hat{C}_n(kP\omega^*+2\omega^2)]+\frac{H_{22}}{4kP^2}\{mP[k\hat{C}_n+(k-1)P]-2k^2\hat{C}_n\hat{C}_n^*\omega^2\}\ . \tag{3.15}$$

Details of this calculation are available in Ref. 20. Equation (3.15) is proportional to the similar coefficient calculated by Wollkind and Segal[5] when the later result is specialized to the case of equal thermal conductivities in both melt and solid.

Wollkind and Segal recognized that both sub- and supercritical evolution of cellular forms are predicted by the result (3.15). We concentrate on the thermophysical properties similar to the lead-antimony (Pb-Sb) system described by Morris and Winegard[21] with the exception that identical thermal properties in melt and solid and zero latent heat were assumed. These properties are listed in Table I along with the dimensionless variables. The sign of the coefficient $G_2^{(1)}$ for this system is shown on Fig. 3 for Peclet numbers 0.8, 8, and 80. The dimensionless wavelength in these figures are scaled with $\lambda^* = 0.01$ cm, as are all calculations presented in Sec. V. At the lowest growth rate ($P = 0.8$) the cellular forms with the highest critical temperature gradient $G_0^{(1)}$ evolved subcritically ($G^{(2)} > 0$) and were initially unstable. Increasing P decreased λ_c and transformed the branch shape to supercritical ($G^{(2)} < 0$); these cellular forms are stable for at least small amplitudes.

TABLE I. Thermophysical properties and dimensionless groups representative of Pb-Sb.

Property	Symbol	Value
Segregation coefficient	k	0.4
Bulk concentration of Sb	$\tilde{c}_\infty$	0.02 wt. %
Slope of liquidus	$\tilde{m}$	-5 K wt. %
Diffusivity	$\mathscr{D}$	2×10^{-5} cm^2/sec
Reference melting temperature	T_m^0	600 K
Capillary length	$\tilde{\Gamma}$	8.2×10^{-9} cm
Reference length scale	λ^*	1×10^{-2} cm
Growth rates	V	1.6×10^{-3}, 1.6×10^{-2}, 1.6×10^{-1} cm/sec
Dimensionless slope of liquidus	m	-1.67×10^{-4}
Capillary constant	Γ	8.2×10^{-7}
Peclet number	P	0.8, 8.0, 80

IV. COMPUTER-AIDED ANALYSIS

A. Formulation

The asymptotic results for the evolution of cellular interfaces are extended to highly deformed shapes by combining numerical solution of Eqs. (3.1) with computer-implemented perturbation methods for tracking multiple steady-state solutions and determining their stability. The calculations presented here are based on the finite-element—Newton technique developed in Ref. 10 for simultaneously calculating the field variables and interface location in a free-boundary problem. To implement this technique the solidification problem is first transformed to a domain with fixed and finite boundaries. We replace the far-field boundary condition (3.1d) with

$$\frac{\partial c}{\partial y}=P(c-c_\infty) \quad \text{at } y=L \ , \tag{4.1}$$

which sets the amount of incoming mass irrespective of back diffusion. Boundary conditions (4.1) and (3.1d) will yield identical results as long as the length L is much greater than the length of the diffusion layer, which scales roughly as P^{-1}. The length L is set to 2.5λ in most of the calculations reported here. Equations (3.1) and (4.1) are transformed to a fixed domain ($0\le\xi\le\lambda$, $0\le\eta\le 1$) using the mapping

$$(x,y)\equiv(\xi,\ h(\xi)+\eta[1-h(\xi)]) \ . \tag{4.2}$$

Introducing Eq. (4.2) into the solidification problem greatly complicates the equation set, but removes the interface shape from setting the domain shape and so reduces $h(\xi)=h(x)$ to a conventional, albeit nonlinear, dependent variable.

The interface shape and concentration field are approximated on the transformed domain by expansions in Lagrangian quadratic $\{\Psi^i(x)\}$ and biquadratic $\{\Phi^i(x)\}$ basis functions constructed on a quadratically discretized domain ($0\le\xi\le\lambda$, $0\le\eta\le 1$). The finite-element expansions are written as

$$\Theta(\xi,\eta)=\sum_{i=1}^{N}\alpha_i\Phi^i(\xi,\eta), \quad h(\xi)=\sum_{i=1}^{M}\beta_i\Psi^i(\xi) \ , \tag{4.3}$$

where the coefficients $\{\alpha_i\}$ and $\{\beta_i\}$ are to be determined and N and M are the numbers of coefficients in each expansion. Following the development in Ref. 10, the field equations and boundary conditions are reduced to a nonlinear algebraic set by Galerkin's method. The equations for steady-state concentration and interface shape are

$$\int_0^\lambda\int_0^1\left[[(L-h)\Phi^i_\xi+(\eta-1)h_\xi\Phi^i_\eta]\left[c_\xi+h_\xi\frac{\eta-1}{L-h}c_\eta\right]+\frac{\Phi^i_\eta c_\eta}{L-h}+P\Phi^i c_\eta\right]d\eta\,d\xi$$
$$+\int_0^\lambda\left[\frac{\Phi^i c_\eta}{L-h}\right]_{\eta=0}d\xi-\int_0^\lambda[\Phi^i P(1-k)c]_{\eta=1}d\xi=0 \ , \tag{4.4}$$

$$\int_0^\lambda\left[\Phi^i(T_I-1)-\frac{\Gamma\Phi^i_\xi h_\xi}{(1+h_\xi^2)^{1/2}}\right]d\xi=0 \ , \tag{4.5}$$

where the equations used are similar to the dimensionless forms in Eqs. (3.1) but with the exponential concentration field for the plane remaining in the solution. In deriving (4.5), we have made use of the condition $\partial h/\partial\xi=0$ at $\xi=0$ and λ. The full set of residual equations (4.4) and (4.5) is conveniently represented as

$$\underline{R}(\underline{x};G)=\underline{0} \ , \tag{4.6}$$

where $\underline{x}^T\equiv(\alpha_1,\alpha_2,\ldots,\alpha_N,\beta_1,\beta_2,\ldots,\beta_M)$ is the vector of all unknown coefficients.

B. Computer-aided analysis and solution stability

The $(N+M)$-dimensional set (4.6) is solved by Newton's method, implemented as described in Ref. 10. In addition to giving more rapid convergence than other iterative schemes for solving nonlinear equations, Newton's method forms the basis for numerically implemented perturbation methods[11–13] for calculating solution families as a parameter is varied, for detecting solution bifurcation, for jumping between solutions, and for determining stability. These methods are analogous to the analytical expansions described in the preceding section, but are performed with base solutions known only in finite-element representation and so are more generally applicable. Specific perturbation schemes have been developed for tracking a simple critical point, either a bifurcation or limit point, in one parameter as a second is varied. This is accomplished by augmenting Eqs. (4.4) and (4.5) with an additional equation for determining a critical point and by considering a parameter (e.g., G) as a dependent variable. Abbott's chord method[22] is employed for solution of the augmented-equation set; see Ref. 12 for details.

The stability of the steadily growing interfaces described by Eq. (4.6) is determined by linear analysis of the evolution of small-amplitude disturbances of the interface shape and concentration field. The full time-dependent versions of (3.1) can be reduced to a set of ordinary differential equations by allowing the coefficients $\{\alpha_i,\beta_i\}$ in (4.3) to be time dependent; these are represented by the form

$$\underline{M}(\underline{x})\frac{d\underline{x}}{dt}=\underline{R}(\underline{x};G) \ , \tag{4.7}$$

where $\underline{M}(\underline{x})$ is a finite-element mass matrix which is

TABLE II. Comparison of lowest critical value $G_c^{(1)}$ computed by finite-element analysis to exact result ($G_c^{(1)}=1.715\,33\times10^{-4}$); $\lambda=2.0$ and $P=0.8$.

Elements in Mesh ξ direction	η direction	$N+M$	$G_c^{(1)}\times10^4$	Percentage error relative to exact result
4	4	90	1.714 47	0.050
4	6	120	1.715 20	0.0076
8	6	238	1.715 20	0.0076
12	8	450	1.715 29	0.0023

dependent on the coefficients $\{\beta_i(t)\}$ because of transformation (4.2). The linear stability of a steady-state solution $\underline{x}_0$ of (4.7) with respect to disturbances written in the same finite-element expansion is examined by considering perturbations of the form

$$\underline{x}(t)\equiv\underline{x}_0+\hat{\underline{x}}\exp(\sigma t)\ , \tag{4.8}$$

where the magnitude of $\hat{\underline{x}}$ is assumed to be small. Substituting (4.8) into (4.7) yields the generalized eigenvalue problem

$$\sigma_i\underline{M}\,\hat{\underline{x}}_i=\underline{J}(\underline{x}_0)\hat{\underline{x}}_i\ , \tag{4.9}$$

for the eigenvalues $\{\sigma_i\}$ and eigenvectors $\{\underline{x}_i\}$, where $\underline{J}(\underline{x}_0)$ is the Jacobian matrix of the nonlinear equation (4.6) evaluated at the known solution $\underline{x}_0$.

The stability of $\underline{x}_0(G)$ can only change at values of G where either a real eigenvalue or the real part of a complex conjugate pair of eigenvalues switches sign. By comparing the linear stability problem with bifurcation equations (see Refs. 13 and 18) it is easy to establish that the first case corresponds to either a simple bifurcation or limit point and the second to a Hopf bifurcation point where a family of time-periodic states branches from the family of steady ones. Changes of stability at bifurcation and limit points detected in this study are analyzed by employing asymptotic results for the derivative of the eigenvalue near the critical point $d\sigma/dG$. These results are presented in Ref. 13 and are not repeated here.

V. LARGE-AMPLITUDE CELLULAR INTERFACES

Families of cellular interface shapes were calculated as a function of the dimensionless temperature gradient G with fixed Peclet number P and wavelength $\lambda=\tilde{\lambda}/\lambda^*$. The accuracy of these calculations was assessed by examining the effect of mesh refinement on both the computed approximations to the critical temperature gradients $G_c^{(i)}$ and the cellular interface shapes computed at large-amplitude deformations. The first critical values $G_c^{(1)}$ computed for $P=0.8$, $\lambda=2.0$, and four meshes are compared to the exact value in Table II. The meshes differed by the number of rectangular elements used to discretize the domain in the ξ and η directions. In each case, the elements were partitioned equally along the interface and were graded near the interface in the η coordinate to help resolve the diffusion layer there. As is seen in Table II, even coarse meshes served for duplicating the linear analysis and the accuracy of the finite-element results improved with mesh refinement, especially in the growth direction. Experience has shown that the finer meshes were necessary for accurate calculations of highly deformed solidification fronts. Most results reported here were performed with a mesh of 10×8 elements graded in both the ξ and η coordinates.

A. Interfaces with wavelength λ and $\lambda/2$.

The families of cellular interfaces which evolved from the lowest two critical values of G for $P=0.8$ and $\lambda=2.0$ are represented on Fig. 4 by the maximum interface deflection Δ computed as

$$\Delta\equiv\max_{0\le x\le\lambda}\{h(x)\}-\min_{0\le x\le\lambda}\{h(x)\}\ . \tag{5.1}$$

For this dimensionless growth rate, $\lambda=2$ was approximately 15% above the critical value $\lambda_c\equiv\tilde{\lambda}_c/\lambda^*$ and was

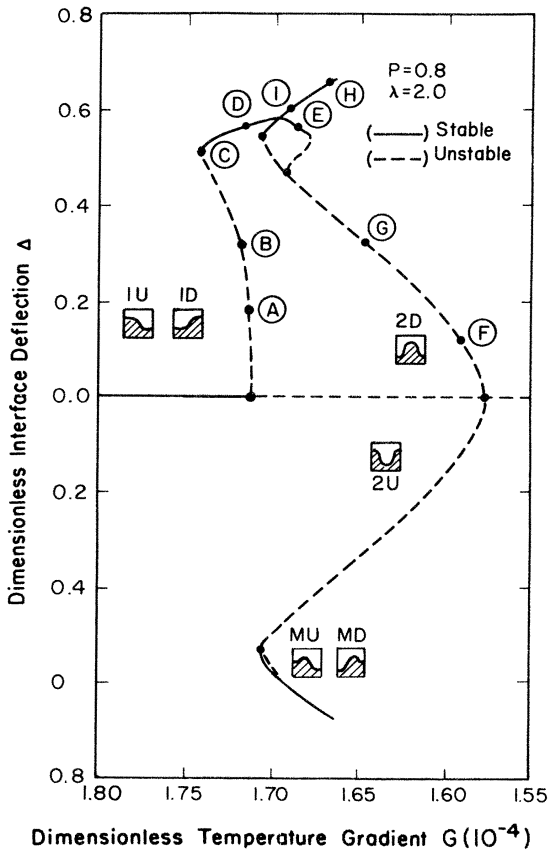

FIG. 4. Families of cellular interfaces for $P=0.8$ and $\lambda=2.0$ as represented by the interface deflection Δ. Letters refer to sample interface shapes in Figs. 5 and 7.

very close to the transition between supercritical and subcritical bifurcation ($G^{(2)}<0$); see Fig. 3(a). The two cellular families branching from the first critical point $G\equiv G_c^{(1)}\simeq 1.715\times 10^{-4}$ had wavelengths $\lambda=2.0$ and evolved almost vertically, but quickly turned to higher values of G, as shown in Fig. 4. Within the accuracy of the finite-element calculations, it was impossible to judge whether this cellular family was supercritical for small values of Δ. These two shape families were identical up to a reflection about the line $x=0$. We have classified them as the $1U$ and $1D$ families where the 1 signifies that the fundamental wavelength of the cells was λ and the U and D denote whether the solid extended into (U) or away from (D) the melt at $x=0$.

The $1U$ and $1D$ families reversed direction at a limit point $G\equiv G_l^{(1)}\simeq 1.745\times 10^{-4}$ and proceeded to lower values of G. At the limit point the cellular forms regained stability and remained stable up to a second limit point $G\equiv G_l^{(2)}\simeq 1.681\times 10^{-4}$ where both families again reversed direction in G. Therefore, stable $1U$ and $1D$ families existed only within the bounds $G_l^{(1)}\le G\le G_l^{(2)}$ on temperature gradient. Sample interface shapes in the $1U$ family are displayed in Fig. 5 for half the wavelength and correspond to the points marked along the first family on Fig. 4. The shapes evolved from nearly sinusoidal forms at low deflections Δ to interfaces with a deep and narrow groove separating a large, almost planar plateau at Δ near 0.5. The most highly deformed interfaces (marked C–E in Fig. 5) developed a depression in the plateau which increased in depth with increasing G. The shapes C and D were predicted to be stable and were similar to the "molar shapes" observed experimentally in Ga-Ge alloys.[23] The grooves in the interface were solute rich as depicted by the isoconcentration curves plotted as Fig. 6. These concentration fields were almost one dimensional, except very near the melt-solid interface.

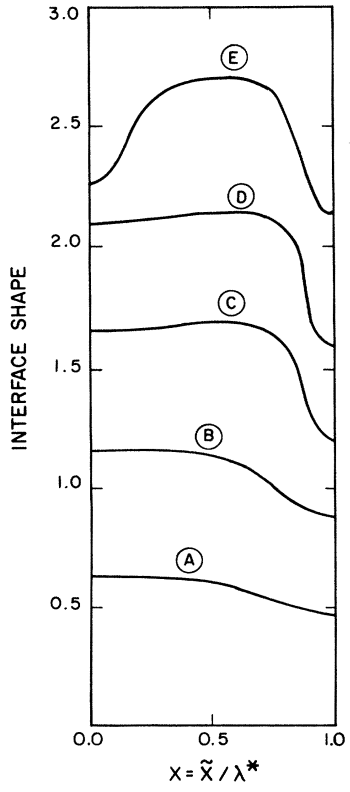

FIG. 5. Sample interface shapes in first families of cellular forms. Letters refer to points shown on Fig. 4.

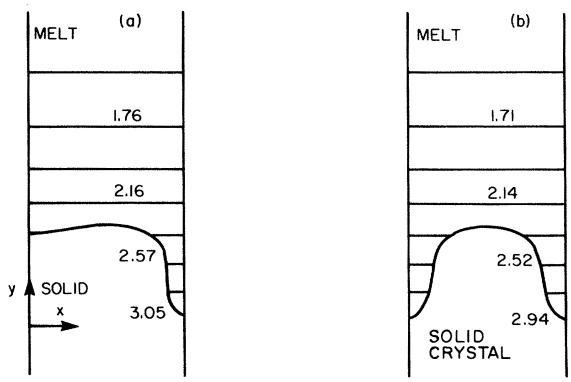

FIG. 6. Concentration fields for representative interface shapes from Fig. 4; (a) corresponds to point D and (b) corresponds to point I.

The two families of cellular forms which bifurcated from the second critical value $G\equiv G_c^{(2)}=1.577\times 10^{-4}$ are also shown in Fig. 4. These families were denoted by $2U$ and $2D$ because each had interfaces with wavelengths of $\lambda/2$ and two complete cells were computed in the spacing $0\le\xi\le 1$. The $2U$ family was composed of cells protruding into the melt at $x=0$ and the $2D$ family contained forms with grooves at this location. Shapes in the two families were identical except for a lateral shift of $x=\pm 0.5$. Even so, the $2U$ and $2D$ families had different nonlinear structure and so are plotted separately on Fig. 4 by reflecting the $2U$ family about the $\Delta=0$ axis. This

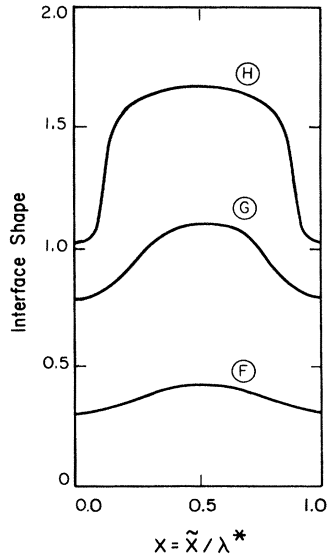

FIG. 7. Sample interface shapes in second family of cellular forms. Letters refer to points shown on Fig. 4.

difference in structure arises when the $2U$ and $2D$ interface shapes are subjected to perturbations which rupture the plane of symmetry about the middle of the cell. Such a disturbance leads to distinct interface shapes for the $2U$ and $2D$ forms.

The $2U$ and $2D$ families bifurcated subcritically for small values of $|G-G_c^{(2)}|$ and contained shapes which were unstable to disturbances with wavelengths of λ and $\lambda/2$. Both families reversed direction at a limit point $G\equiv G_l^{(3)}\simeq 1.71\times 10^{-4}$ for highly deformed shapes and evolved to higher values of G. Representative interface shapes in the $2D$ family are shown in Fig. 7. With increasing Δ the interfaces formed the deep grooves noted in shapes belonging to the $1U$ and $1D$ families, but at half the wavelength.

Just before the limit point in the $2D$ family (at $G\equiv G_s^{(1)}\simeq 1.694\times 10^{-4}$), the $1U$ and $1D$ families merged with the $2D$ forms at a simple bifurcation point. At this value of G the depression in the "molar-shaped" interfaces became identical with the groove in the $2D$ forms, thus effectively halving the interfacial wavelength. For the $2D$ forms, stability with respect to a single mode was regained at both the secondary bifurcation and limit points. Interfaces along the supercritical portion of the $2D$ family then were stable to all disturbances that preserved the fundamental wavelength λ.

The $2U$ family evolved identically to the $2D$ forms. Although no connection between the $2U$ and either the $1U$ or $1D$ forms was found, a secondary bifurcation was located on the $2U$ family before the limit point $G_l^{(3)}$, as shown in Fig. 4. The interfaces in the two new families looked like

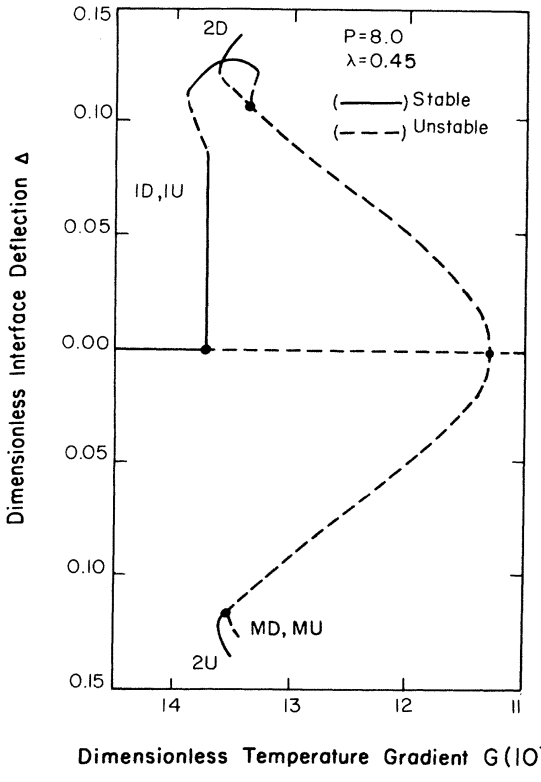

FIG. 8. Families of cellular interfaces for $P=8.0$ and $\lambda=0.45$ as represented by the interface deflection Δ.

a mixture of $2U$ with $1U$ and $1D$ forms and were denoted as MU and MD where (M) signified the mixed symmetry of the family. These forms were predicted to be unstable. Beyond the limit point the $2U$ forms were stable to all distances with wavelength λ. Overall, the nonlinear evolution and stability results for the first four families predicted an abrupt transition between interfaces with wavelength λ and $\lambda/2$ occurring at a temperature gradient near $G_l^{(2)}$.

Changing the dimensionless growth velocity P shifted the bifurcation structure shown on Fig. 4 with respect to G, but did not alter the connectivity between the families. This point is demonstrated in Fig. 8 for the first two shape families and $P=8.0$. Several changes occurred at this high growth rate. As shown on Fig. 3(b), the wavelength for the most dangerous disturbance decreased to $\lambda_c\simeq 0.40$. The finite-element calculations were carried out for $\lambda=0.45$, where the $1U$ and $1D$ families bifurcated supercritically (to lower G). Therefore, a slight decrease in the temperature gradient from $G_c^{(1)}\simeq 1.375\times 10^{-3}$ led to a smooth transition from the planar solidification front to stable, small-amplitude sinusoidal shapes. These stable forms existed only in the range $1.375\times 10^{-3}\geq G\geq 1.371\times 10^{-3}$; at the lower limit $G_l^{(1)}\simeq 1.371\times 10^{-3}$ the family reversed direction in G and lost stability. Except for this small region of stable interface shapes near $G_c^{(1)}$, the evolution of all four shape families was qualitatively similar to the results for $P=0.8$.

B. Evolution of nonlinear structure with varying wavelength

Although it is most meaningful to perform the nonlinear analysis near the most dangerous wavelength λ_c, the details of the nonlinear structure shown in Figs. 4 and 8 are best understood through calculations for varying $\lambda=\tilde{\lambda}/\lambda^*$. The reason for this is clearly seen by examining Figs. 3(a)–3(c). By strictly geometrical arguments it is readily proved that for some wavelength $\lambda\equiv\lambda_d$ greater than λ_c, the critical points $G_c^{(1)}$ and $G_c^{(2)}$ corresponding to the development of families with wavelength λ_d and $\lambda_d/2$ coincide, and for higher values of λ the first critical point results in bifurcation to forms with wavelength $\lambda/2$. This particular wavelength $\lambda\equiv\lambda_d$ marks a multiple critical point in the terminology of bifurcation theory[18] and signals the possibility of secondary bifurcations in the vicinity of the critical value $G=G_c^{(1)}=G_c^{(2)}$. The connection between the $1U$, $1D$, and $2D$ families is such a bifurcation point.

The shape families originating from the highest two critical values ($G_c^{(1)}$ and $G_c^{(2)}$) are represented in Fig. 9 for $P=0.8$ and wavelengths of 2.60, 2.70, and our estimated value of $\lambda=\lambda_d\simeq 2.64$. At $\lambda=2.60$ the ordering of the single- and double-wavelength families was the same as for $\lambda=2.0$; however, the secondary bifurcation between the $1U$, $1D$, and $2D$ families and between the mixed modes MU and MD had moved below the limit point $G_l^{(1)}$ to small values of the deflection. The $1U$ and $1D$ families evolved subcritically between temperature gradients $G_c^{(1)}$ and $G_s^{(1)}$.

As the wavelength was increased toward λ_d, the four bifurcation points ($G_c^{(1)}$, $G_c^{(2)}$, $G_s^{(1)}$, and $G_s^{(2)}$) all coalesced

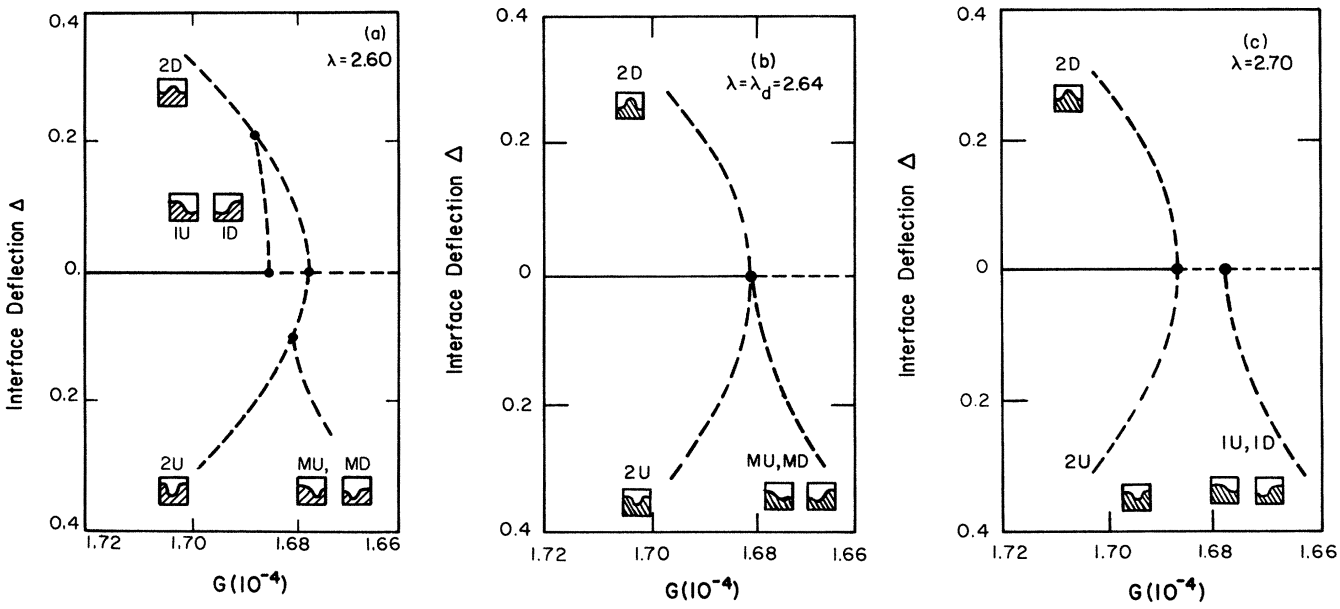

FIG. 9. Families of cellular interfaces for $P=0.8$ as the wavelength is varied through the double critical point; the figures correspond to wavelengths of (a) 2.60, (b) 2.64, and (c) 2.70.

and the extent of the $1U$ and $1D$ families was shortened. At the double point $\lambda\equiv\lambda_d\simeq 2.64$ the $1U$ and $1D$ families disappeared and left only the $2U$, $2D$, MU, and MD families evolving from $G=G_c^{(1)}=G_c^{(2)}$. The critical values for the $2D$ and $2U$, and $1D$ and $1U$ families, changed order for wavelengths greater than λ_d. The MU and MD families, which had been mixed mode at their bifurcation points, became pure $1U$ and $1D$ when they bifurcated from the planar interface shapes; however, they had a component of the half-wavelength form for even small deflections. The $2D$ and $2U$ families evolved subcritically with respect to G and the $1D$ and $1U$ families developed supercritically, as shown on Fig. 9(c) for $\lambda=2.70$.

The transition through a double critical point with

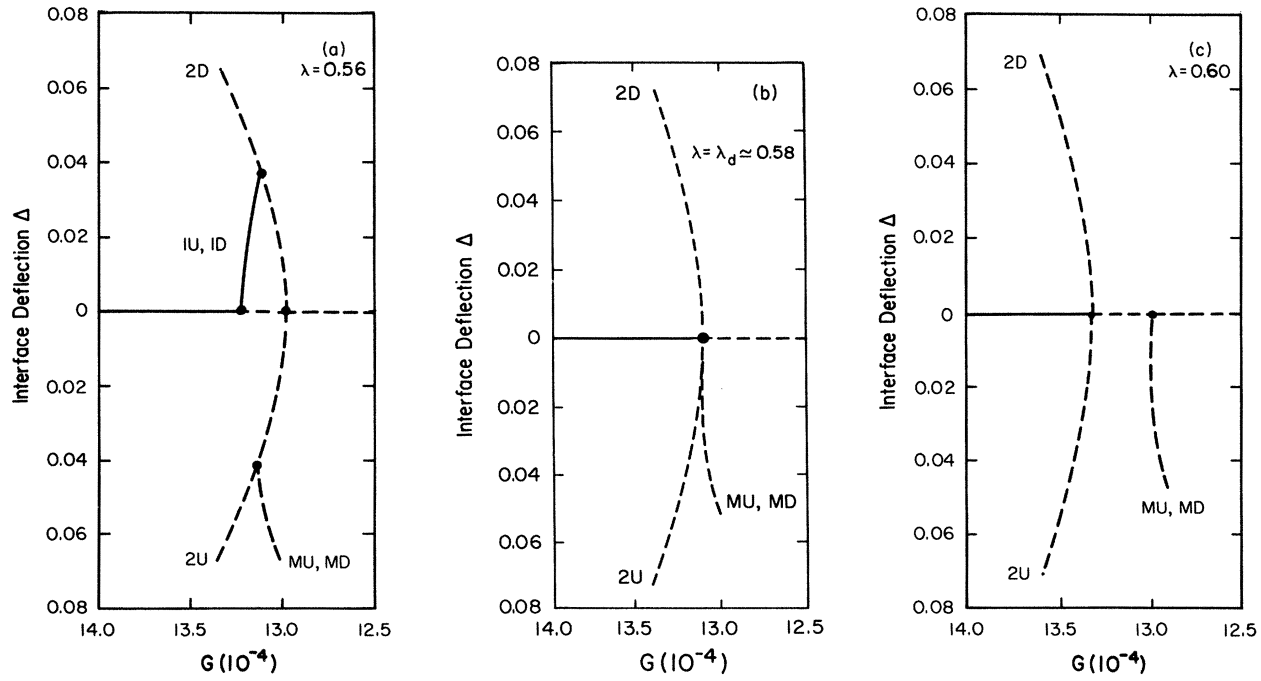

FIG. 10. Families of cellular interfaces for $P=8.0$ as the wavelength is varied through the double critical point; the figures correspond to wavelengths of (a) 0.50, (b) 0.58, and (c) 0.60.

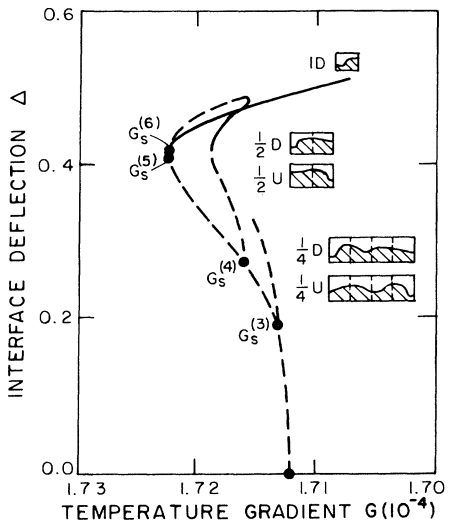

FIG. 11. Families of interfaces with wavelength 2λ and 4λ which branch from the $1U$ family for $P=0.8$. Only the lower part of the 4λ curve is shown.

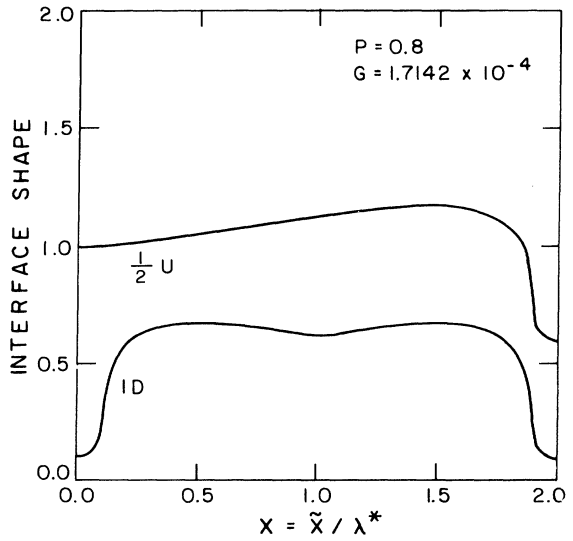

FIG. 12. Sample interface shapes in the $1D$ and $\frac{1}{2}U$ families for $P=0.8$ and $G=1.71\times10^{-4}$.

changes in the wavelength described above was qualitatively preserved for $P=8.0$ as shown in Fig. 10 for values of λ less than, equal to, and greater than λ_d.

C. Secondary bifurcation to interfaces with longer wavelengths

Families of interfaces with longer wavelength branched from the planar interface at lower temperature gradients than either the $1U/1D$ or $2U/2D$ families and were unstable to several shape instabilities; see Fig. 3(a). However, these long-wavelength forms did play a significant role in setting the stability of the finite-amplitude $1U$ and $1D$ interfaces. Calculations for the $1U$ family allowing for cellular forms of wavelength 2λ and 4λ, are summarized in Fig. 11. These calculations used a mesh of only 16×3 elements in the x and y directions and so are only approximate. Pairs of secondary bifurcation points were detected between the $1U$ family and new interfaces composed of a mixture of elements with wavelengths λ, 2λ, and 4λ. Two new families of wavelength 4λ evolved from the first bifurcation point $G\equiv G_s^{(3)}\simeq1.72\times10^{-4}$ and are believed to rejoin this family at the second point $G\equiv G_s^{(6)}\simeq1.71\times10^{-4}$. Stability of the $1U$ forms was lost to disturbances of wavelength 4λ at the first branch point, but was regained at $G=G_s^{(6)}$. Since this portion of the $1U$ family was already unstable to shorter wavelength perturbations, the predictions for stable $1U$ forms in Sec. V A were unchanged. Bifurcating families which evolve from and rejoin a single primary family have been seen in natural convection[13] and meniscus-shape[24,25] problems.

The second and third bifurcation points ($G_s^{(4)}$ and $G_s^{(5)}$) along the $1U$ family marked the branching of new families composed of λ and 2λ components; we denoted these $\frac{1}{2}D$ and $\frac{1}{2}U$. The $1U$ forms were unstable to disturbances with wavelength 2λ only between these two bifurcation points. As depicted in Fig. 11, each of these new shape families evolved initially to lower values of G and turned back to rejoin the $1U$ family. Again, the region of stable, large-amplitude $1U$ forms was not changed by these longer-wavelength shapes. The $\frac{1}{2}D$ and $\frac{1}{2}U$ forms were stable to disturbances of wavelength λ and 2λ in a short region between two limit points but were unstable to disturbances with wavelength 4λ. Sample interface shapes from the $\frac{1}{2}U$ family are compared in Fig. 12 to $1D$ shapes at approximately the same value of G and $P=0.8$.

VI. DISCUSSION

The complicated interconnections of the cellular interface families computed here point to the rich mathematical structure that is involved in modeling the morphology of a melt-solid interface. The families constructed by asymptotic and computer-aided analysis (see Figs. 4, 8, and 9) represent planes taken from the full set of steady, two-dimensional solutions to the one-sided model parametrized by temperature gradient G, fundamental wavelength λ, and interface deflection. These results suggest that large-amplitude, two-dimensional cellular morphologies, which are at least stable to two-dimensional disturbances, exist for an extended range of wavelengths and temperature gradients near the critical values for instability of the planar shape. McFadden and Coriell[26] have calculated similar two-dimensional shapes for a more complicated solidification model which accounts for changes in the temperature field caused by interface shape.

Long-wavelength two-dimensional instabilities seemed to play only a minor role in determining the shape of the cellular interfaces at large amplitude. For wavelengths up to 4 times the critical value, cellular forms with this symmetry bifurcated from and rejoined the primary family with wavelength λ. We suspect the same pattern of secon-

dary bifurcation and recombination to occur for families with longer wavelengths. Kerszberg,[27] and Mather and Dee,[28] have both used asymptotic expansions to determine the change in fundamental wavelength with amplitude. Both predict that the wavelength increases with decreasing G. Our results suggest that these analyses have detected the secondary bifurcation between the primary wavelength λ_c and longer waveforms, but are not valid at large enough amplitude to detect the recombination predicted here.

The existence of the large-amplitude cellular shapes was independent of whether these families branched sub- or supercritically with respect to G, as seen by comparing the results for Peclet numbers of 0.8 and 8.0. Not surprisingly, the amplitude expansion (Sec. III) accurately predicted only the evolution of slightly deformed interfaces and did not give any indication of the commonalities between the nonlinear structures for the sub- and supercritical cases. Wollkind and Segal[5] conjectured that this difference was linked to the cellular to dendritic transition in interface morphology. We have seen no evidence in our calculations for the development of bumps or arms along the cells which seem to mark predendritic growth. Moreover, preliminary eigenvalue calculations for the stability of these interfaces have shown no bifurcations to time-periodic growth where predendritic growth would be expected to occur.

More likely, the transition to dendritic growth involves three-dimensional cellular forms which have been disallowed in our calculations. The pictures sketched by Morris and Winegard[22] point to a sequence of interface shapes progressing from steady two-dimensional, to steady three-dimensional, and finally to time-periodic, three-dimensional morphologies. Finite-element calculations for three-dimensional interfaces, although expensive, may uncover these transitions.

The existence of the second-order critical point at $\lambda \equiv \lambda_d$ gave a mechanism for reducing the nonlinear connectivity of the first ($1U$ and $1D$) and second ($2U$ and $2D$) bifurcating families to small amplitude where the results of an amplitude expansion are meaningful. Asymptotic analyses for double critical points have been carried out for other transport problems,[14–16] but have not been pursued here. Instead, we used only the concept of the double point to identify the parametric region ($\lambda \simeq \lambda_d$) for reducing the secondary bifurcations to small amplitude, where the finite-element analysis was extremely accurate. Elsewhere,[29] these amplitude expansions have been used to explain the role of a grain boundary along an interface as a primary imperfection to the connectivity of the cellular interface families presented here. Third-order critical points which exist when three-dimensional interfaces are considered may offer a mechanism for reducing the nonlinear interactions responsible for dendritic growth to a region amenable to asymptotic analysis.

ACKNOWLEDGMENTS

This research was supported by the Materials Processing Program of the U. S. National Aeronautics and Space Administration, by the Information Processing Center at Massachusetts Institute of Technology, and by the Mobil Foundation.

APPENDIX

The coefficients appearing in Eq. (3.14) are

$$H_{20} \equiv 0 , \tag{A1}$$

$$C_{20} \equiv k(k-1)(1-2k\omega_n^*/g)/2 , \tag{A2}$$

$$H_{22} \equiv \{(k\omega_n^* P+2\omega_n^2)(k/g)+[\omega_{2n}^*+P(k-1)](1-2k\omega_n^*/g)/2-kP/2\}/PD_{22} , \tag{A3}$$

$$C_{22} \equiv \{[1/2-(g\omega_n^*+\omega_n^2)/gP][kP/g-3k\omega_n^2\Gamma/(k-1)mP]+k\omega_n^*/g-1/2\}k^2(k-1)/D_{22} , \tag{A4}$$

where

$$D_{22} \equiv (\omega_{2n}^*/P+k-1)[kP/g-2k\omega_n^2\Gamma/(k-1)mP]-k , \tag{A5}$$

$$g \equiv \omega_n^*+P(k-1) . \tag{A6}$$

---

*Author to whom correspondence should be addressed.

[1]J. W. Rutter and B. Chalmers, Can. J. Phys. 31, 15 (1953).
[2]W. W. Mullins and R. F. Sekerka, J. Appl. Phys. 34, 323 (1963).
[3]W. W. Mullins and R. F. Sekerka, J. Appl. Phys. 35, 444 (1964).
[4]R. T. Delves, *Theory of Interface Stability, in Crystal Growth,* edited by B. R. Pamplin (Pergamon, Oxford, 1975).
[5]D. Wollkind and L. Segel, Philos. Trans. R. Soc. London Ser. A 268, 351 (1970).
[6]J. S. Langer and L. A. Turski, Acta Metall. 25, 1113 (1977).
[7]J. S. Langer, Acta Metall. 25, 1121 (1977).
[8]J. D. Hunt, in *Solidification and Casting of Metals,* edited by J. Hunt (The Metals Society, London, 1979).
[9]J. S. Langer, Rev. Mod. Phys. 52, 1 (1980).
[10]H. M. Ettouney and R. A. Brown, J. Comput. Phys. 49, 118 (1983).
[11]H. B. Keller, *Numerical Solution of Bifurcation and Nonlinear Eigenvalue Problems,* in *Applications of Bifurcation Theory,* edited by P. H. Rabinowitz (Academic, New York, 1977).

[12]L. H. Ungar and R. A. Brown, Philos. Trans. R. Soc. London A 306, 347 (1982).
[13]Y. Yamaguchi, C. J. Chang and R. A. Brown, Philos. Trans. R. Soc. London Ser. A (to be published).
[14]J. P. Keener, Stud. Appl. Math. 55, 187 (1976).
[15]P. Hall and I. C. Walton, J. Fluid Mech. 90, 377 (1979).
[16]S. Rosenblat, J. Fluid Mech. 122, 895 (1982).
[17]D. P. Woodruff, *The Solid-Liquid Interface* (Cambridge University Press, London, 1973).
[18]G. Iooss and D. D. Joseph, *Elementary Stability and Bifurcation Theory* (Springer, New York, 1980).
[19]D. D. Joseph, Arch. Rat. Mech. Anal. 51, 295 (1973).
[20]L. H. Ungar, Ph.D. thesis, Massachusetts Institute of Technology, 1984.
[21]L. R. Morris and W. C. Winegard, J. Cryst. Growth 1, 245 (1967).
[22]J. P. Abbott, J. Comput. Appl. Math. 4, 19 (1978).
[23]D. E. Holmes and H. C. Gatos, J. Appl. Phys. 52, 4 (1981).
[24]R. A. Brown and L. E. Scriven, Phys. Rev. Lett. 45, 180 (1980).
[25]R. A. Brown and L. E. Scriven, J. Colloid Interface Sci. 78, 528 (1980).
[26]G. B. McFadden and S. R. Coriell, Physica D (to be published).
[27]M. Kerszberg, Phys. Rev. B 27, 3909 (1983).
[28]G. Mathur and G. Dee (unpublished).
[29]L. H. Ungar and R. A. Brown (unpublished).